Tellus
SERIES B
CHEMICAL
AND PHYSICAL
METEOROLOGY
PUBLISHED BY THE INTERNATIONAL METEOROLOGICAL INSTITUTE IN STOCKHOLM

Tellus (2009), 61B, 79–95
Printed in Singapore. All rights reserved

TELLUS

Spectral absorption coefficients and imaginary parts of refractive indices of Saharan dust during SAMUM-1

By T. MÜLLER[1]*, A. SCHLADITZ[1], A. MASSLING[1,†], N. KAADEN[1], K. KANDLER[2] and A. WIEDENSOHLER[1], [1]*Leibniz Institute for Tropospheric Research, 04318 Leipzig, Germany;* [2]*Applied Geosciences Department, Darmstadt University of Technology, 64287 Darmstadt, Germany*

(Manuscript received 12 March 2008; in final form 22 September 2008)

ABSTRACT

During the SAMUM-1 experiment, absorption coefficients and imaginary parts of refractive indices of mineral dust particles were investigated in southern Morocco. Main absorbing constituents of airborne samples were identified to be iron oxide and soot. Spectral absorption coefficients were measured using a spectral optical absorption photometer (SOAP) in the wavelength range from 300 to 800 nm with a resolution of 50 nm. A new method that accounts for a loading-dependent correction of fibre filter based absorption photometers, was developed. The imaginary part of the refractive index was determined using Mie calculations from 350 to 800 nm. The spectral absorption coefficient allowed a separation between dust and soot absorption. A correlation analysis showed that the dust absorption coefficient is correlated (R^2 up to 0.55) with the particle number concentration for particle diameters larger than 0.5 μm, whereas the coefficient of determination R^2 for smaller particles is below 0.1. Refractive indices were derived for both the total aerosol and a dust aerosol that was corrected for soot absorption. Average imaginary parts of refractive indices of the entire aerosol are 7.4×10^{-3}, 3.4×10^{-3} and 2.0×10^{-3} at wavelengths of 450, 550 and 650 nm. After a correction for the soot absorption, imaginary parts of refractive indices are 5.1×10^{-3}, 1.6×10^{-3} and 4.5×10^{-4}.

1. Introduction

Mineral dust plays an important role in Earth's climate system (Haywood and Bougher, 2000; IPCC, 2007). It is essential to understand the processes of formation, transport and modification of dust because Saharan mineral dust can travel thousands of kilometres across the Atlantic (Kaufman et al., 2005). The interaction of mineral dust and solar and terrestrial radiation is a complex field. Minerals can be strong or weak light absorbers depending on their mineralogical composition and the wavelength of light. Besides the composition, the quantity of the dust-induced radiative forcing also depends on the mass and number size distribution of suspended dust, the vertical distribution and the albedo of the underlying surface (Sokolik and Toon, 1996; Tegen et al., 1996). Mineral dust aerosols can thus lead to either cooling or warming of the Earth's atmosphere.

For radiative transfer calculations, the particle absorption and scattering coefficients are necessary prerequisites. These properties are functions of the size and shape of dust particles as well as of the complex refractive index, which depends on the mineralogical composition. The investigation of the imaginary part of the refractive index, which is responsible for the absorption, is a main issue for dust characterizations with respect to optical properties.

An overview of refractive indices of dust is given by, for example, Sokolik and Toon (1999). In the recent years, optical dust properties have been measured in the laboratory (e.g. Linke et al., 2006) and in airborne field experiments (Haywood et al., 2001; Haywood et al., 2003). However, to date, a characterization of mineral dust with respect to physical and optical properties in a source region of mineral dust is missing.

As shown by Sokolik and Toon (1999), the imaginary part of the refractive index is strongly variable in the spectral range from the ultraviolet (UV) to the near-infrared (NIR). In recent years, it was shown how iron oxides, which are responsible for the reddish colour of many dusts (e.g. Arimoto et al., 2002; Alfaro et al., 2004; Fialho et al., 2006), influence the spectral optical properties of mineral dust. Therefore, the investigation of spectral optical properties is of special interest. The lack of spectral refractive indices for dust particles is a weak point in modelling the impact of mineral dust on the Earth's radiation budget. Whereas measurements of the absorption coefficients at few discrete wavelengths are a first estimate of quantifying the total absorption of suspended dust, a differentiation between the

*Corresponding author.
e-mail: thomas.mueller@tropos.de
†Now at: National Environmental Research Institute, Aarhus University, 4000 Roskilde, Denmark
DOI: 10.1111/j.1600-0889.2008.00399.x

major compounds is difficult. Measurement devices for measuring the absorption coefficient at discrete wavelengths are the Aethalometer (Hansen et al., 1984) and the Particle Soot Absorption Photometer (PSAP, Radiance Research; Seattle, WA). The PSAP was modified to measure the particle absorption coefficient at three wavelengths (Virkkula et al., 2005) and the Aethalometer (model AE 31) measures the particle absorption coefficient at seven discrete wavelengths. Aethalometer loading and scattering corrections were reported by Weingartner et al. (2003), Arnott et al. (2005) and Schmid et al. (2006). In the recent years, the Aethalometer was used to identify dust events (e.g. Collaud Coen et al., 2004; Fialho et al., 2006).

The absorption coefficient is a basic parameter to derive the imaginary part of the refractive index. The analysis of spectral refractive indices in a large spectral range is a powerful tool for estimating chemical compositions and thus the sources of aerosols. To close this gap and deriving spectral absorption coefficients, a spectral optical absorption photometer (SOAP) was employed during the intense field study SAMUM-1 to measure the absorption coefficient from 300 to 800 nm with a spectral resolution of 50 nm. The absorption photometer primarily measures the optical transmission and reflection of a fibre filter, while loading this filter with aerosol particles. A radiative transfer model, based on a ray-tracing model, was developed to calculate the absorption coefficient.

Not only data evaluation of in situ measurements but also remote sensing techniques, for example, LIDAR, sun-photometry and satellite observation, benefit from the derived spectral refractive indices.

2. Methodology and measurement methods

2.1. Location and measurement setup

The Saharan mineral dust experiment was conducted in southern Morocco in 2006. A field station with in situ observations of microphysical and optical aerosol properties was located near the village Tinfou, close to the hotel 'Porte au Sahara' (30°14′15″ N, 5°36′29″W, 684 m a.s.l.), which is approximately 35 km southeast of the city Zagora. Another field station was placed at the airport of Quarzazate (coordinates 30.93°N, 6.91°W). Lidar measurements and aircraft activities were done at the airports of Quarzazate and Casablanca. The aircrafts 'Partenavia' (Type P68B) and the research aircraft 'Falcon' (Falcon 20-E) of the German Aerospace Center (DLR) were flying patterns over southern Morocco and also over both field stations.

The in situ measurements for characterizing optical properties at the field station Tinfou were performed in an air conditioned container with temperatures around 22 °C. An aerosol inlet system (PM10) was mounted above the roof of the container and had an aerodynamic cut-off diameter of 10 μm. Aerosol was fed into the container using a vertical aerosol tube. Inside of the container, the aerosol flow was divided into several flows. Downstream the aerosol splitting, the aerosol was dried to relative humidities lower than 20% using Nafion® dryers and diffusion dryers. Special care was taken to avoid gravitational losses in sampling lines, especially for instruments measuring particles larger 1 μm in diameter.

In the following, we summarize the instruments and methods that were used to measure spectral absorption coefficients and to derive the imaginary part of refractive indices.

The particle number size distribution was measured using a Differential Mobility Particle Sizer (DMPS; Birmili et al., 1999), in the mobility size range from 20 to 800 nm. An Aerodynamic Particle Sizer (APS; model 3321, TSI Inc., St. Paul, USA) was used for measuring particle number size distributions from 0.53 to 10 μm in aerodynamic diameter. The DMPS was connected to the aerosol inlet by a 2-m horizontal line. Gravitational losses were estimated to be negligible for particles up to 800 nm in diameter. The APS was placed directly below the inlet to avoid gravitational losses for particles up to 10 μm in diameter. The particle number size distributions of DMPS and APS were combined using an inversion scheme yielding the particle number size distribution from 20 nm up to 10 μm of volume-equivalent particle diameters. This inversion scheme accounts for density and dynamic shape factors of particles and applies a multiple charge correction for particles larger than 800 nm in the DMPS. A description of this method is given by Schladitz et al. (2008).

Particle scattering and backscattering coefficients were measured with an integrating nephelometer (model 3563, TSI Inc., St. Paul, USA) at wavelengths of 0.45, 0.55 and 0.7 μm. The nephelometer measures the scattering in a limited angular range from 7° to 170°. The measured values were corrected for the so-called truncation error by a method given by Anderson et al. (1996) to retrieve the total particle scattering coefficient.

A PSAP was used to measure the particle absorption coefficient at 530 nm. A calibration and correction for particle scattering for PSAP was done using the method given by Bond et al. (1999). It was found that for mineral dust, a further correction scheme (Section 2.2) had to be applied to account for a loading effect. The connection of nephelometer and PSAP to the inlet required a 2-m horizontal tube and several bendings in the tube. Sampling line losses were estimated and Mie calculations using particle number size distributions and refractive indices given by Schladitz et al. (2008) were used to estimate correction factors for particle scattering and absorption coefficients. The correction factors were used to compensate for the sampling line losses and thus to provide scattering and absorption coefficients corresponding to the PM10 inlet cut-off.

The spectral absorption coefficient was measured using a SOAP. The SOAP measures the optical transmission and reflection of a fibre filter, whereas the filter is loaded with particles. The spectrometer covers a spectral range from 300 to 800 nm with 50 nm resolution. An inversion scheme based on a ray-tracing method is introduced in Section 2 and was used to calculate the particle absorption coefficient and to estimate a scattering

parameter, which is strongly related to the particle scattering coefficient. This scattering parameter is used for a correction of the cross sensitivity of the absorption measurement to particle scattering. The SOAP was placed directly below the aerosol inlet. Thus, no sampling line losses due to gravitational settling were expected.

The SOAP was employed first during the SAMUM-1 experiment in Morocco in 2006. A description of this instrument is given in Section 2.2.3, after introducing the basics of measuring the particle absorption coefficient using a PSAP. The absorption coefficients derived by the SOAP were calibrated by an intercomparison with PSAP and nephelometer, respectively. Sampling line losses of the instruments were taken into account before calibration.

2.2. *Method of measuring the absorption coefficients and loading correction using ray tracing*

2.2.1. Effects of multiple scattering in fibre filters on the measurement of particle absorption. Aerosol particles scatter and absorb light. The situation is, however, more complex if the particles are embedded in a filter. Whereas the filter matrix has a low absorption coefficient, the scattering coefficient is rather large so that multiple scattering takes place. This scattering leads to an optical path length in the filter, which is larger than the geometrical thickness of the filter. If the filter is loaded with absorbing particles by sucking a column of air of length ds through the filter, the attenuation of the light beam is enhanced because of the increased path length. A correction is therefore needed, which accounts for this effect. If the filter is loaded with highly scattering particles, the effective path length in the filter is increased and can lead to a further enhancement of the absorption of the probe.

2.2.2. Principle of measurement for the PSAP. The method for measuring the particle absorption coefficient is given here for the PSAP. However, the PSAP data evaluation had to be modified as shown later. The PSAP measures the temporal change of the transmittance, while a fibre filter (Pallflex, E70–2075W) is being loaded. The filter is illuminated by an LED from the particle-loaded side. A detector is placed behind the fibre filter. From the change of the optical transmission the absorption coefficient is calculated by

$$\sigma'_{\mathrm{abs}} = \frac{A\ \Delta t}{V}\ \ln\left(\frac{I_0}{I}\right), \tag{1}$$

where A is the area of the sample spot, I/I_0 is the change in transmittance during the time period Δt in which the volume V is drawn through the filter. The spot area and volume flow have to be corrected by a method given by Bond et al. (1999).

The values reported by the PSAP include an empirical correction function:

$$\sigma_{\mathrm{PSAP}} = \frac{\sigma'_{\mathrm{ap}}}{2\,(0.5398\ \tau + 0.355)}. \tag{2}$$

It accounts for the enhancement effect due to multiple scattering in the particle-filter system. The correction depends on the actual loading with particles, which is measured by the transmission $\tau = I/I_0$. A further correction introduced by Bond et al. (1999) also takes a cross sensitivity to particle scattering into account by using

$$\sigma_{\mathrm{ap}} = \frac{\sigma_{\mathrm{PSAP}} - K_1 \cdot \sigma_{\mathrm{sp}}}{K_2}. \tag{3}$$

Equation 3 is a linear correction of the scattering artefact. Limitations of the linear corrections were given by Bond et al. (1999):(1) PSAP shows decreased response to scattering when the filter is loaded with non-absorbing particles. (2) The response to scattering increases when absorbing particles are present on the filter. (3) The response to scattering depends on particle size and thus on the ratio of backscattering to scattering.

To overcome the limitations of a linear correction scheme, we have set up a ray-tracing model (Monte Carlo simulation). This model was used to simulate the response of absorbing and scattering particles and to develop an improved correction method.

2.2.3. Setup of the Spectral Optical Absorption Photometer (SOAP). The SOAP was developed for measuring the spectral absorption coefficient, with similar technique used for the PSAP. The main difference to the PSAP is that the SOAP uses a light source with an emission of light from the UV to the NIR. The detection of light is done by an optical spectrometer. Additional to the measurement of transmission, a second detection channel was set up which measures the reflectance of the particle-loaded filter. The sensing head of the SOAP is shown in Fig. 1.

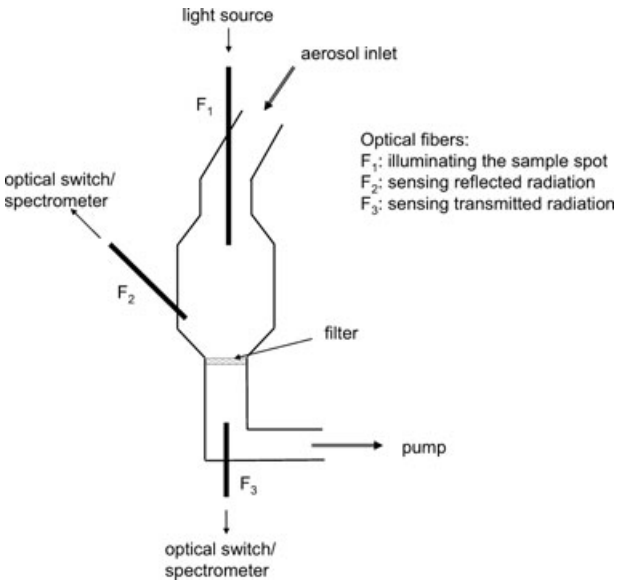

Fig. 1. Sketch of the sensing head of SOAP. Shown are the aerosol flow through the sensing head and particle filter, and the optical illumination and sensing the transmitted and reflected radiation using optical fibres.

Key components of the SOAP are: (1) A deuterium–halogen lamp (Avantes, AvaLight-DHS-DUV) with high emission in the UV. (2) An optical spectrometer (Control Development Inc., CDI2DMPP-UV-VIS) covering the wavelength range from 200 to 800 nm with an optical resolution of 25 nm. The wavelength range from 200 to 300 nm is not useable for SOAP because of a low signal-to-noise ratio. The entrance slit of the spectrometer was removed and the end face of an optical fibre acts as entrance slit. This modification causes a rather low wavelength resolution but is necessary to minimize the optical losses and to ensure a high signal-to-noise ratio. Additionally, each measured spectrum was smoothed to reduce noise. The effective wavelength resolution after smoothing is 50 nm. (3) The measurements were done in a measurement head that allows collecting particles on a fibre filter (Pallflex E70/2075W), to illuminate the sample spot with an optical fibre and to measure the transmittance and reflectance of the particle loaded filter. (4) An optical switch selects either the transmittance or the reflectance channel to measure the spectral intensity with the spectrometer.

While loading the filter with particles, the spectral transmitted and reflected intensities I_τ and I_ρ are measured. The measured transmittance can be used to calculate a spectral absorption coefficient in a similar way as for the PSAP. To make the SOAP comparable to the PSAP, the diameter of the sample spot is 6 mm ($\sim$5 mm for PSAP) and the aerosol flow is 1 lpm (1 to 2 lpm for PSAP).

The uncertainty (95% confidence level) was determined by measuring a time-series of absorption coefficients using filtered, particle-free air. For a 10 min averaging time, the uncertainties at the wavelengths of 300, 600 and 700 nm are 0.6, 0.3 and 0.5 Mm^{-1}, respectively.

Because of the known problems with the scattering correction, as discussed for the PSAP, a new correction method was developed for SOAP using ray tracing.

2.2.4. Ray-tracing model. The geometry of the filter-particle system simulated by a ray-tracing model is shown in Fig. 2. The filter has three layers, the filter matrix and a composite layer of filter matrix, including embedded particles, and a backing layer, which ensures the mechanical stability of the filter. In case of an unloaded filter, the composite layer has the same optical properties as the filter matrix.

The filter is illuminated from the top by a light beam with initial intensity I_0. Inside the filter, scattering and absorption of light occur by collected aerosol particles, as well as by the fibre filter. The processes of scattering and absorption were implemented to trace photons through the filter.

The principle of ray tracing was given by Prahl et al. (1989). Light scattering changes the direction of light propagation without any change of the total energy of the incident radiation. The mean free path between two scattering events is given by $\mu = 1/\sigma_{\mathrm{sca}}$, where σ_{sca} is the scattering coefficient of the filter. The scattered energy per solid angle in direction $(\theta_\mathrm{s}, \phi_\mathrm{s})$ is given by the phase-function $p(\theta_\mathrm{i}, \phi_\mathrm{i}, \theta_\mathrm{s}, \phi_\mathrm{s})$ with the initial direction $(\theta_\mathrm{i}, \phi_\mathrm{i})$ of the incoming photons.

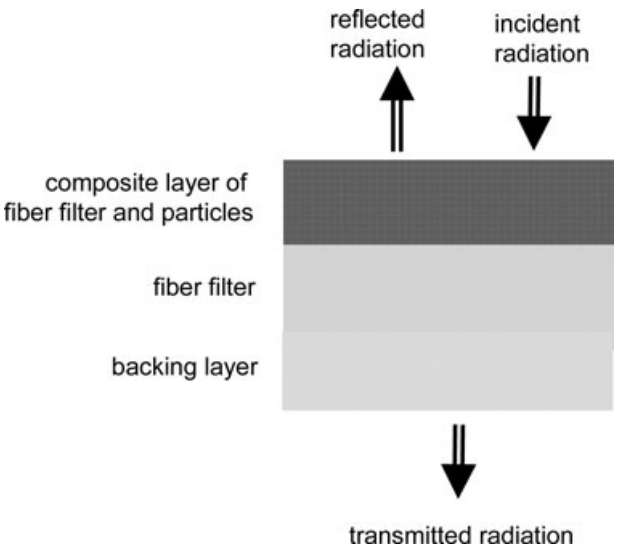

Fig. 2. Schematic drawing of a particle-filter system with three layers. The filter is illuminated from the particle-loaded side. Also shown are reflected and transmitted radiations.

In contrast, absorption removes energy from the light beam. The amount of removed energy is given by the absorption coefficient σ_{abs}. After travelling a distance of ds, the intensity I(ds) amounts to

$$I(\mathrm{d}s) = I(0)\ \mathrm{e}^{-\sigma_{\mathrm{abs}}\mathrm{d}s}. \tag{4}$$

The optical depth is defined as

$$OD = \sigma_{\mathrm{abs}}\mathrm{d}s. \tag{5}$$

The ray tracing was implemented for a multiple layer system. Each layer is defined by absorption and scattering coefficients and the asymmetry parameter g. The phase-function is assumed to be a Henyey–Greenstein phase-function (Henyey and Greenstein, 1941), which only has the asymmetry parameter as variable. The asymmetry parameter was chosen to be 0.7 that equals to a relative hemispherical backscattering of 0.084. The reason for using Henyey–Greenstein phase function for both—the filter and the particle scattering–is that this phase function is easy to implement in a ray-tracing model. The output of the ray-tracing model is the scattered energy per solid angle in steps of 10° and the total flux for both the transmission and reflection at the boundaries of each layer.

2.2.5. Determination of optical properties of fibre filters. We had, however, to characterize the unloaded filter before using the ray-tracing model for simulation of particle loading. This characterization was done by measurements of the angular intensity distribution function and the total attenuation by the filter. These data were used to calculate the ratio of forward scattering to backscattering and the fraction of absorbed energy. Afterwards,

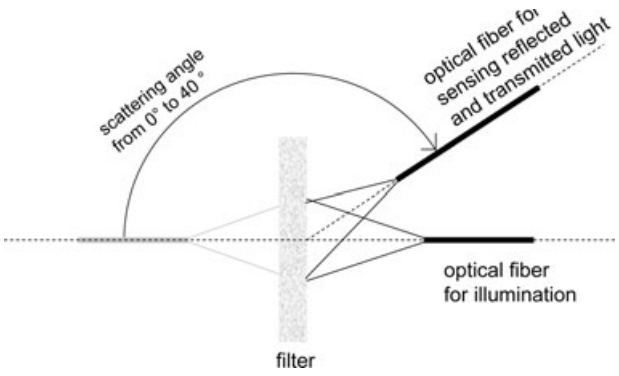

Fig. 3. Schematic of the spectral, polar photometer. The sensing fibre can be rotated from 0° (transmission) to 140° (reflection). The centre of rotation is in the middle of the filter and on the centre line of the illumination fibre.

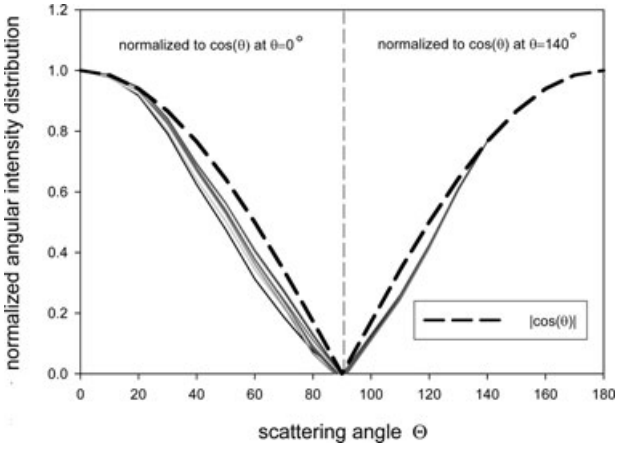

Fig. 4. The normalized angular intensities distribution for the total filter system. The different lines are for discrete wavelengths between 250 and 800 nm. Each curve was normalized separately.

the effective absorption and scattering coefficients of the filter were estimated. These coefficients are denoted as 'effective coefficients' because the scattering by fibre filters is neither homogenous nor isotropic. The ray-tracing model, however, assumes homogeneous and isotropic scattering.

The filter itself consists of three layers as described before. We estimated the thickness of the particle filter to be 200 μm and the thickness of the backing to be 100 μm using an optical microscope, whereas the filter layer is white and the backing is slightly grey. We measured the optical parameters for the total filter and for the backing layer after carefully removing the filter layer from its backing.

The scattering intensities $S(\theta, \lambda)$ were measured by a polar photometer (see Fig. 3) in the wavelength range $\lambda = 250$–800 nm for scattering angles θ between 0° and 140° in steps of 10°. The measured angular intensity distribution is shown in Fig. 4. The intensities scattered in forward direction are normalized to unity at 0° scattering angle. The backward scattering is measured up to angles of 140°. This branch is normalized to $|\cos(140°)|$ at 140°. In addition, a function of the form $|\cos(\theta)|$, which is for a perfectly diffuse scattering medium, is shown. The normalized branches of angular intensity functions for different wavelengths differ by less than 10% for forward scattering and 5% in case of backscattering. Figure 5 shows the ratio $S(0°,\lambda)/S(140°,\lambda)$ for the total filter and for the backing only. The backscattering of the backing is much lower compared with that of the total filter.

The relative scattered radiation by the fibre filter $S_F(\lambda)$, which is defined as the ratio of incident radiation to the sum of forward and backward scattered radiation, was measured using an integrating sphere (see Fig. 6). The integrating sphere collects diffusely transmitted and diffusely backscattered radiation. The relative scattered radiation was determined by measuring the intensity with and without a filter. The spectral relative scattered radiations $S_F(\lambda)$ for the backing layer and the total filter are shown in Fig. 7.

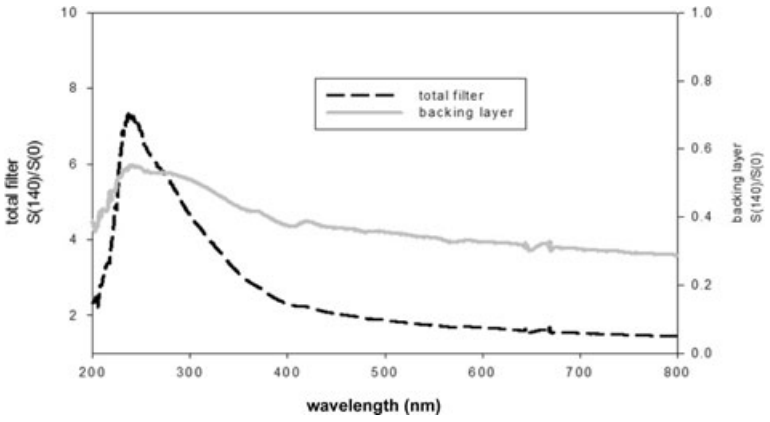

Fig. 5. Ratio of scattered intensities at 140° (S(140)) to 0° (S(0)) versus the optical wavelength.

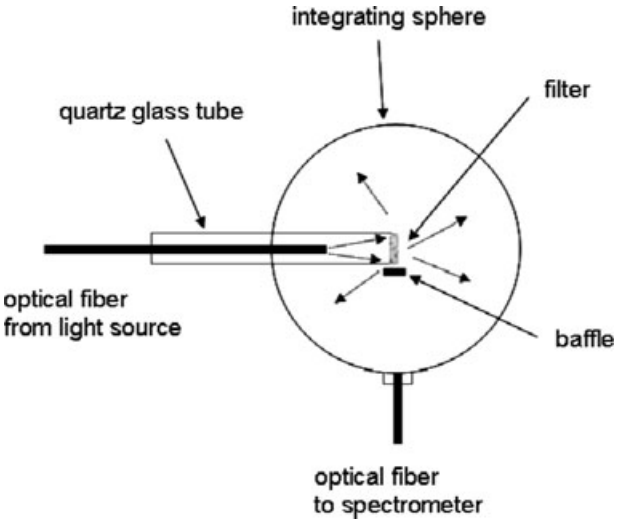

Fig. 6. Setup for measuring the total scattered radiation using an integrating sphere.

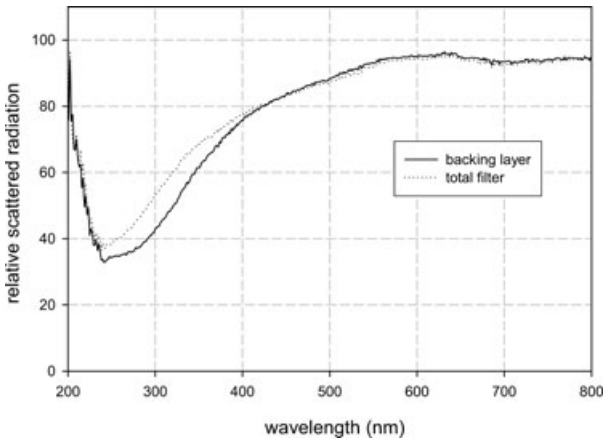

Fig. 7. Relative scattered radiation in per cent for the total filter and the backing only. Differences to 100% are caused by absorption of the filter material.

An iterative algorithm was applied to find the effective absorption and scattering coefficient of the fibre filter until the ray tracing simulated $S_F(\lambda)$ and $S(0^\circ,\lambda)/S(140^\circ,\lambda)$ fit to the experimental results within an accuracy of $\pm 2\%$. First, the absorption and scattering coefficients of the backing were determined by simulating only the backing layer. Then, the absorption and scattering coefficients of the filter layer were determined by simulating the total filter system with the known properties of the backing layer. This procedure was done for several wavelengths. The resulting effective absorption and scattering coefficients of the fibre filter are shown in Fig. 8.

2.2.6. Simulation of attenuation and reflectance by particles. The effective thickness of the particle-filter layer was estimated for the simulation of the particle loading. We calculated that

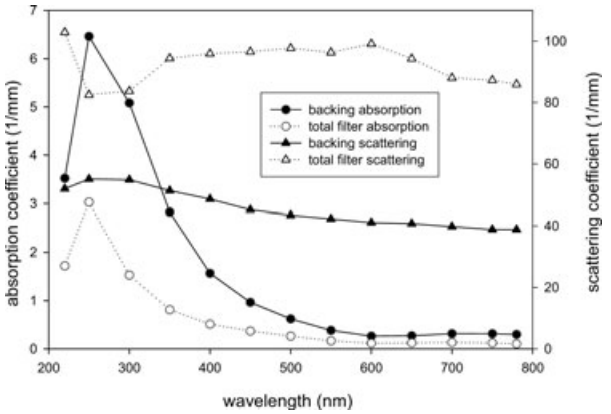

Fig. 8. Calculated effective absorption and scattering coefficients of a blank filter.

a sampling efficiency of 99% and an exponential decay of the particle concentration along the cross-section of the filter results to an effective thickness of 16 μm. The effective layer thickness was defined as the median of the particle concentration profile.

The scattering and absorption coefficients of filter and particles were added for the particle-filter layer. This simple approach of adding optical properties does not consider interference effects of fibres and particles. Therefore, the ray-tracing model requires a 'model calibration'.

Measurable quantities in a multiple scattering system are the diffusely transmitted and reflected intensities. In the following, we use the subscripts τ and ρ to indicate diffuse transmission and diffuse reflection. The attenuation and reflectance are determined by simulation of the transmitted and reflected intensities I_τ and I_ρ in relation to the intensities measured for an initially unloaded filter $I_{\tau,0}$ and $I_{\rho,0}$. The attenuation and reflectance are defined as

$$ATN = -\ln(I_\tau / I_{\tau,0}) \tag{6}$$

and

$$REF = -\ln(I_\rho / I_{\rho,0}). \tag{7}$$

In general, the ray-tracing model assumes that the attenuation and reflectance are functions of the optical depth, which is caused by the 'true' optical depth of particle absorption (OD_{abs}), scattering (OD_{sca}) and backscattering (OD_{bsca}):

$$ATN = r_\tau(OD_{\mathrm{abs}}, OD_{\mathrm{sca}}, OD_{\mathrm{bsca}}) \tag{8}$$

and

$$REF = r_\rho(OD_{\mathrm{abs}}, OD_{\mathrm{sca}}, OD_{\mathrm{bsca}}), \tag{9}$$

whereas the optical depths are defined as $OD_x = \sigma_x L$ with $x = \{\mathrm{sca}, \mathrm{abs}, \mathrm{bsca}\}$. L is the length of the column of air, which is sucked through the filter. The functions r_τ and r_ρ are called

the response functions of the filter-particle system and describe the interaction of particles in a multiple scattering system.

The choice of constant particle penetration affects the sensitivity to particle absorption, scattering and backscattering. Particles near the surface scatter light back out of the filter towards the light source without a further scattering process. Backscattering, which takes place deeper in the filter, would be accompanied by further scattering processes. Thus, the response to backscattering depends on the particle penetration depth.

Simulating ATN and REF in the four-dimensional space with the three optical depths and the wavelengths is very time consuming. A simulation of one pair of ATN and REF values requires the simulation of 10^6 photons to have a sufficient counting statistics for photons. This calculation takes about 5 min using a 2 GHz desktop PC. Simulation of at least 10 values for each of the four dimensions requires a total computing time of about 34 d.

Because of the unknown dependence of REF on the particle penetration depth and the high computing time, we decided to simplify the model by eliminating the backscattering in eqs. 8 and 9. We assumed a constant ratio of backscattering to total scattering. A similar simplification is included in the scattering correction function introduced by Bond et al. (1999) for the PSAP (eq. 3) because the correction solely depends on the total particle scattering coefficient.

For simulations, we have chosen a ratio of backscattering to total scattering of 0.1. This ratio was measured by a total scattering and backscattering nephelometer during the SAMUM-1 field campaign (Schladitz et al., 2008). The calibration shown in this publication thus is valid for aerosols with a relative backscattering ratio of 0.1.

2.2.7. Constraining the ray-tracing model to experimental calibration. For low particle loadings, we introduce sensitivities. The sensitivities are defined as the measured properties (attenuation and reflectance) divided by the desired optical quantities (optical depth of absorption and scattering) for low loading. The four sensitivities are

Sensitivity of attenuation to absorption particles:

$$s_{ATN,\mathrm{abs}} = \lim_{OD_{\mathrm{abs}}\to 0} \frac{r_\tau(OD_{\mathrm{abs}}, 0)}{OD_{\mathrm{abs}}}. \tag{10}$$

Sensitivity of attenuation to scattering particles:

$$s_{ATN,\mathrm{sca}} = \lim_{OD_{\mathrm{sca}}\to 0} \frac{r_\tau(0, OD_{\mathrm{sca}})}{OD_{\mathrm{sca}}}. \tag{11}$$

Sensitivity of reflectance to absorption particles:

$$s_{REF,\mathrm{abs}} = \lim_{OD_{\mathrm{abs}}\to 0} \frac{r_\rho(OD_{\mathrm{abs}}, 0)}{OD_{\mathrm{abs}}}. \tag{12}$$

Sensitivity of reflectance to scattering particles:

$$s_{REF,\mathrm{sca}} = \lim_{OD_{\mathrm{sca}}\to 0} \frac{r_\rho(0, OD_{\mathrm{sca}})}{OD_{\mathrm{sca}}}. \tag{13}$$

The four sensitivities are merged to a sensitivity matrix $\bar{\bar{s}}$ with

$$\bar{\bar{s}} = \begin{pmatrix} s_{ATN,\mathrm{abs}} & s_{ATN,\mathrm{sca}} \\ s_{REF,\mathrm{abs}} & s_{REF,\mathrm{sca}} \end{pmatrix}. \tag{14}$$

The sensitivities are useful to constrain the ray-tracing model. For a 'calibration' of this model, we introduce the superscripts 'm' for the output of the model calculation and 'e' for the results of experiments. The intention is to compare the sensitivity matrices $\bar{\bar{s}}^{\mathrm{m}}$ and $\bar{\bar{s}}^{\mathrm{e}}$, and to adjust the model to the experimental data.

The sensitivity matrix calculated using the ray-tracing model amounts at a wavelength of 530 nm (interpolated between 500 and 550 nm) to

$$\bar{\bar{s}}^{\mathrm{m}} = \begin{pmatrix} 1.867 & 0.059 \\ 3.33 & -0.025 \end{pmatrix}. \tag{15}$$

To obtain a sensitivity matrix from experimental results, we used data from different experiments and data from literature. The derivation of the sensitivity matrix from experimental data is shown in the following.

The matrix element s^{e}_{11} is the sensitivity to purely absorbing particles, when measuring ATN in transmission. s^{e}_{11} is calculated using the calibration derived by Bond et al. (1999). The value following Bond et al. (1999) is given by $s^{\mathrm{e}}_{11} = 1.79 \times 0.87 \times 1.22 = 1.89$. The first multiplicand is the sensitivity calculated by the PSAP firmware at transmission 1, which corresponds to low filter loading. The second term accounts for a further correction of the spot size, because the PSAP firmware uses a wrong spot size in the calculation, and we have to undo this effect. The third term is a calibration constant (K_2), which was found by Bond et al. (1999).

We measured the change of attenuation and reflectance, while loading a filter with strongly absorbing soot particles (Printex 75, Degussa GmbH). The ratio of the reflectance to attenuation was determined to be 1.3, which leads to the matrix element $s^{\mathrm{e}}_{21} = s^{\mathrm{e}}_{11} \times 1.3 = 2.47$.

The cross sensitivity to particle scattering is taken again from the correction function given by Bond et al. (1999). It can be shown (using the formulae given in Bond et al. (1999)) that the cross sensitivity is given by $s^{\mathrm{e}}_{12} = K_1 \times 0.9 \times s^{\mathrm{e}}_{11}$, where $K_1 = 0.02$ and S^{e}_{11} accounts for the transmittance correction function. K_1 was derived for use of a scattering coefficient measured by a nephelometer (TSI Inc., model 3563) at 550 nm. Because of the truncation error (Anderson et al, 1996) of this nephelometer type, the measured scattering coefficient is smaller by about 10% than the total particle scattering coefficient. Thus, a factor of 0.9 was included. The sensitivity amounts to $s^{\mathrm{e}}_{12} = 0.018 \times s^{\mathrm{e}}_{11} = 0.0325$.

The sensitivity s^{e}_{22} is given by the ratio of attenuation to reflectance for purely scattering material. The ratio of attenuation to reflectance was measured in a laboratory

experiment to be –4.34 for ammonium sulphate, which leads to $s^{e}_{22} = -\frac{1}{4.34} \times s^{e}_{12} = -0.0075$.

The overall sensitivity matrix for experimental data is

$$\bar{\bar{s}}^{e} = \begin{pmatrix} 1.89 & 0.0325 \\ 2.47 & -0.0075 \end{pmatrix}. \quad (16)$$

We defined a calibration matrix γ with $\overline{\overline{s^{e}}} = \overline{\overline{\gamma}} \cdot \overline{\overline{s^{m}}}$. The calibration matrix results to

$$\overline{\overline{\gamma}} = \begin{pmatrix} 1.02 & 0.55 \\ 0.74 & 0.30 \end{pmatrix}. \quad (17)$$

Using this matrix, the ray-tracing model is constrained to experimental data for strongly absorbing and purely scattering aerosol. The matrix elements γ_{11} andγ_{21}, which are related to sensitivities to particle absorption, are close to unity, respectively, ≈26% lower. The calibration matrix elements γ_{12} and γ_{22}, which are related to particle scattering, are much smaller than unity. The values of the calibration matrix indicate that interaction of absorbing particles embedded in a filter matrix is well described by the model in contrast to particle scattering.

Differences between modelled and measured sensitivities might be caused by several factors. The model assumes a homogenous distribution of particles in the particle layer of a constant thickness. From theory, it is clear that the number concentration of deposited particles should follow an exponential decay in respect to the penetration depth. The deeper the particles are deposited in the filter the more their inherent phase-function is covered by the multiple scattering of the filter matrix. Particles deposited near the surface can modify the total phase function of the composite layer. The reflection strongly depends therefore on particle properties and on their penetration depth. Another reason for the differences might be an interference effect of particle and fibre filter scattering, which is not taken into account in the model. The simple approach of adding optical properties is a first assumption, and the use of the calibration matrix implies that the interference effect can be compensated by a simple factor.

2.2.8. Determination of absorption coefficients. To obtain the particle absorption and scattering coefficients from measurements of ATN and REF, an inversion scheme of eqs. 8 and 9 including the calibration matrix, has to be applied. An iterative inversion algorithm was tested to be unambiguous for $OD_{abs} < 1$ and $OD_{sca} < 10$. The results of the inversion were stored in look up tables LT_{abs} and LT_{sca} as function of *ATN* and *REF* with

$$\begin{aligned} OD_{abs} &= LT_{abs}(\gamma_{11} \times ATN, \gamma_{12} \times REF) \text{ and} \\ OD_{sca} &= LT_{sca}(\gamma_{21} \times ATN, \gamma_{22} \times REF). \end{aligned} \quad (18)$$

To include the wavelength dependence of the absorption by the filter material, the ray-tracing simulations and the inversion were done for wavelengths from 300 to 800 nm in steps of 50 nm. The corrected optical depths can be calculated by interpolation between entries of the look up tables and interpolation between wavelengths. The absorption coefficient is calculated by the difference of two consecutive measurements divided by the length of the column of air (ΔL) that is sucked through the filter during the two measurements:

$$\sigma_{abs}(t) = \frac{OD_{abs}(t) - OD_{abs}(t - \Delta t)}{\Delta L} \quad (19)$$

2.3. Modified scattering correction for the PSAP

There are two methods for correcting the absorption coefficients reported by the PSAP. The first method to correct the scattering artefact for the PSAP was given by Bond et al. (1999). The second method is to correct PSAP data with the ray-tracing method and using the scattering coefficient given by a nephelometer. Fig. 9 shows the ratio of ray-tracing corrected absorption coefficients to absorption coefficients, which were corrected using the method given in Bond et al. (1999). In cases of low single scattering albedo ($\omega_0 < 0.5$) with $\omega_0 = \sigma_{sca}/(\sigma_{sca} + \sigma_{abs})$, both methods agree very well. The deviation for high single scattering albedo is, however, significant. At a single scattering albedo of 0.9 and a transmission of 0.8, the absorption coefficient calculated using the Bond correction is higher by 20% compared with the ray-tracing method.

A comparison of single scattering albedo calculated by the nephelometer scattering and the PASP absorption coefficients measured during the SAMUM experiment is shown in Fig. 10. The PSAP data were corrected with both correction methods. It can be seen that the correction shown in Bond et al. (1999) shows a saw-tooth structure when changing the filter. This structure is mostly reduced by using the ray-tracing method. It has to be noted that both methods agree for low loadings independent of the single scattering albedo. This result follows from the fact that the calibration constants γ were calculated using the calibration given by Bond et al. (1999) at low loadings. The ray-tracing method is thus not a real calibration of absorption photometers,

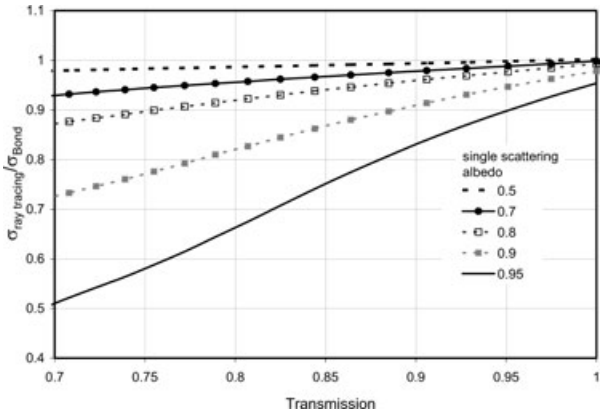

Fig. 9. Ratio of absorption coefficients calculated by ray tracing to absorption coefficients calculated using the method shown in Bond et al. (1999) for different single scattering albedos versus the filter transmission.

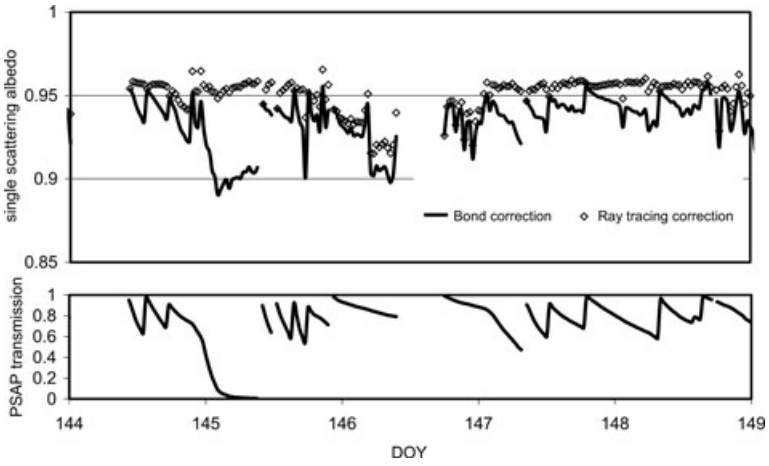

Fig. 10. Single scattering albedo calculated using the method shown by Bond et al. (1999) and the ray-tracing corrected PSAP values. Data were collected during the SAMUM field campaign.

but a modified correction of loading effects dependent on single scattering albedo.

2.4. Calibration of SOAP for mineral dust

The SAMUM-1 field campaign was the first field experiment using the SOAP. A post calibration was done by comparing the absorption coefficients of the SOAP at the wavelength of 530 nm to the absorption coefficient measured by the PSAP. PSAP data were corrected using the ray-tracing method to correct for loading effects.

The linear regression line between SOAP versus PSAP has a slope of 1.12 and a coefficient of determination R^2 of 0.88. This correction factor was used as a post calibration for the SOAP. Also the scattering coefficients determined by the SOAP and the truncation-corrected nephelometer scattering were correlated. The slope of this correlation was 0.86 and the coefficient of determination was $R^2 = 0.87$. This recovery of the scattering coefficient using the SOAP method lends confidence in the scattering correction applied to the absorption coefficients.

3. Results

3.1. Evaluation of spectral refractive indices

Average spectral absorption coefficients measured by SOAP are shown in Fig. 11 for four time periods. These four periods are representative in terms of optical properties for most cases during the SAMUM-1 field campaign. The average particle number size distribution for these periods is given in Fig. 12. For a better differentiation between cases with high and low dust conditions, the particle number size distribution was split into two parts, a dust and a fine mode with fitted logarithmic normal particle number size distributions with average mean diameters of 0.4 and 0.08 μm, respectively. This separation is not only a size separation but represents rather more a separation into groups of different chemical composition (Kaaden et al., 2008).

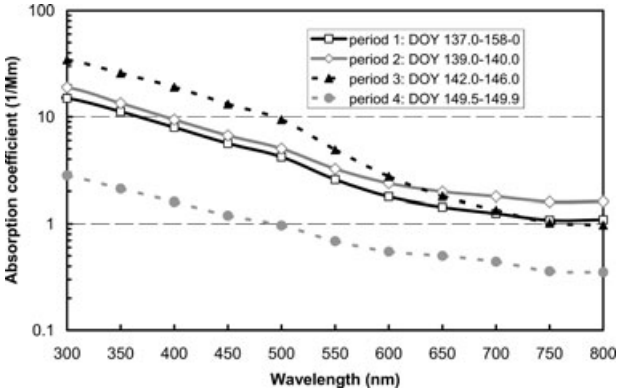

Fig. 11. Spectral particle absorption coefficients for several periods.

Period 1 covers three weeks of continuous measurements from day of year (DOY) 137 to 158. Period 2 is a one-day average, which is represented by a particle number size distribution similar to the average of the entire field experiment (Period 1). A four-day period with a relatively high concentration of dust mode particles is given by Period 3. During this period, times with extremely high dust concentrations during sandstorms were excluded to avoid problems with inlet and sampling line losses. A case with very low dust concentration is given in Period 4. Periods 3 and 4 are of special interest because the investigation of optical properties of dust mode and fine mode particles is easiest for these two extreme cases.

Optical properties of particle populations are often given by the Ångström absorption and scattering exponents (Ångström, 1964). The Ångström absorption exponent is defined as

$$\alpha = -\frac{\ln\left(\sigma_{\mathrm{abs}}(\lambda_1)/\sigma_{\mathrm{abs}}(\lambda_2)\right)}{\ln\left(\lambda_1/\lambda_2\right)}. \tag{20}$$

Ångström absorption exponents were derived from absorption spectra at wavelengths of 450 and 700 nm. Periods 1 and 2 show similar absorption spectra with Ångström absorption exponents of 3.4 and 3.0, respectively. Also the particle number size dis-

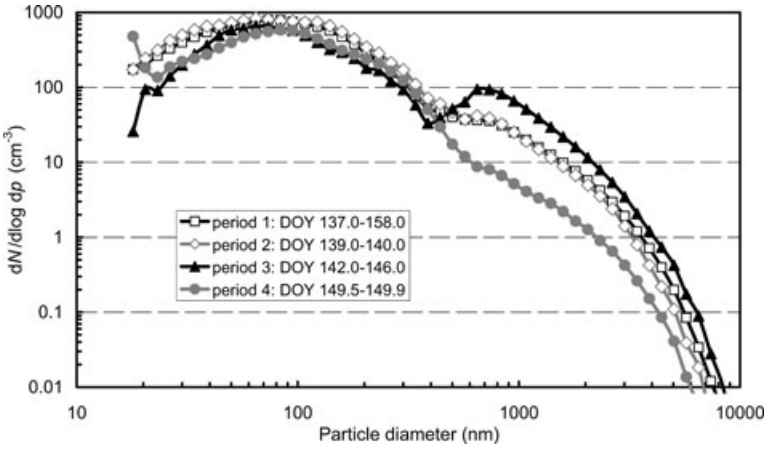

Fig. 12. Particle number size distribution for the four selected periods.

tributions for both cases were similar. The effective radii, which are three times the third moment divided by the second moment of the particle number size distribution, were 0.67 and 0.56 μm for Periods 1 and 2, respectively. During Period 3, a stronger wavelength dependence occurred with $\alpha = 5.13$. The respective effective radius was determined to be 0.78 μm. This strong spectral dependence can be typically found for high iron oxide concentrations (e.g. Fialho et al., 2006). The lowest values for the Ångström absorption exponent with $\alpha = 2.25$ and effective radius with 0.41 μm were observed for Period 4. The dependence of the Ångström absorption exponent leads to the assumption that there is at least one more absorbing component in the fine particle mode with a spectrally rather constant refractive index like that of soot.

To determine the optical properties of dust mode particles, a method was introduced for separation of the measured absorption spectra into two parts, the dust and the fine mode absorption. This method is presented later in Sections 3.3 and 3.4.

The imaginary part of the complex refractive index ($m = n - ik$) was calculated for the four periods using an inversion scheme (RI-inversion) based on a Mie scattering code. This RI-inversion is subject to several constraints. The real part of the refractive index was assumed to be 1.53. This value often is used for mineral dust in literature (Hess et al., 1998; Shettle and Fenn, 1979; Sokolik and Toon, 1999), and was also derived for the SAMUM-1 campaign by Schladitz et al. (2008). Another constrain is the assumption of spherical particles for Mie scattering calculations. Effects for non-spherical particles were not considered.

The algorithm basically consists of four steps: (1) forward calculation with a starting value of the imaginary part of refractive index and using the particle number size distributions shown in Fig. 12; (2) comparing measured and calculated absorption coefficients and modifying the imaginary part of refractive index; (3) repeating steps 1 and 2 until the measured and calculated imaginary parts of the refractive index fit and (4) repeating steps 1 to 3 for all wavelengths.

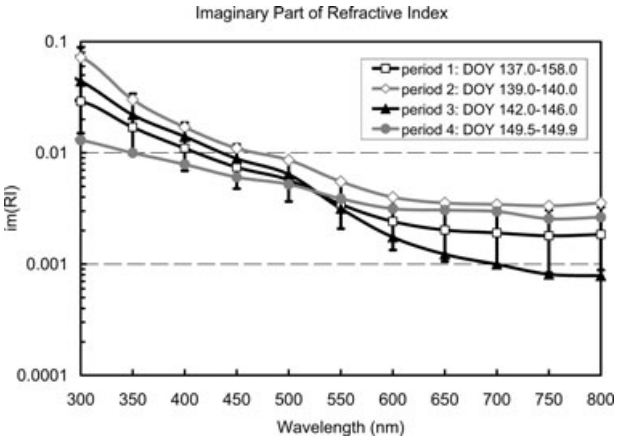

Fig. 13. Spectral imaginary part of refractive indices of the total aerosol for the four time periods. Error bars are only shown for Period 1.

The resulting spectral imaginary parts of refractive index are shown in Fig. 13. It can be seen that the imaginary part of refractive index has its lowest value at long wavelengths for the dust case. In this case, the increase of the imaginary part of refractive index towards shorter wavelengths was most pronounced. This finding is typical for hematite (e.g. Sokolik and Toon 1999). During Period 4, there is only a relatively weak spectral dependence. The other two periods could be interpreted as a mixture (in terms of absorption) of the two extreme cases.

3.2. *Laboratory measurements of Saharan dust and hematite*

Microphysical properties of Saharan dust and hematite were measured in a laboratory experiment. The dust sample was dispersed by an air stream and fed into a mixing chamber. Instruments for measuring the optical and physical properties were connected to several output ports of the chamber. The particle

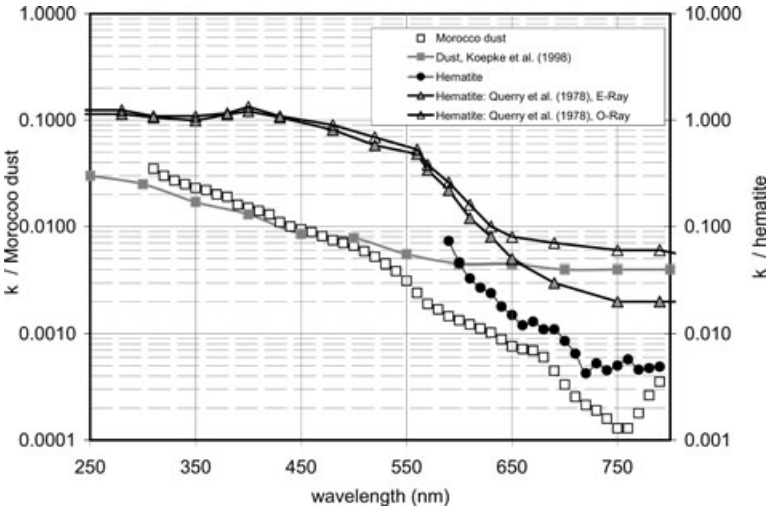

Fig. 14. Imaginary part of refractive index of Saharan dust and hematite measured during laboratory experiments. Also shown are imaginary parts of refractive indices from literature.

number size distribution was measured using a DMPS and an APS. The conversion of measured mobility diameters to diameters of a volume equivalent sphere is given by Schladitz et al. (2008). For that calculation, values for the dynamic shape factor of $\chi = 1.2$ and for the particle density of $\rho = 5.1$ and 2.7 g cm^{-3} for iron oxide containing mineral dust, respectively, were used.

Absorption spectra were measured by the SOAP, and scattering coefficients were measured using a three-wavelength nephelometer (TSI, model 3565). Using the ray-tracing correction and the RI-inversion scheme, the imaginary part of the refractive index was derived. Figure 14 shows imaginary parts of the refractive indices derived by the laboratory experiment, for dust given by Hess et al. (1998) and for hematite given by Sokolik and Toon (1999). The imaginary part of the refractive index k of hematite was only calculated from 590 to 790 nm, because the RI-inversion method failed for high values of k, which is the case for smaller wavelengths. Both measured spectra show a minimum of the imaginary part and the absorption coefficient at the wavelength of 750 nm. This spectral feature can be used to identify dust, particularly hematite. It has to be taken into account that the iron oxides hematite and goethite have similar optical properties (Balkanski et al., 2007). Thus, we cannot distinguish between these two iron oxides. The ratio of absorption coefficients at wavelengths of 650 and 750 nm was found to be 2.8. If the ratio is smaller than 2.8, then a second (spectrally broad) absorber is needed to explain the spectral absorption coefficient. A ratio of 1.15 corresponds to an Ångström absorption exponent of 1.0, which is typical for externally mixed soot.

3.3. Partitioning of refractive indices with respect to absorbing compounds

The ratio of absorption coefficients at wavelengths of 650 and 750 nm can be used to separate the absorption into two parts, which are the absorption by iron oxide containing dust (in this case hematite) and the absorption by a second soot-like absorber. The ratios from 2.8 to 1.15 are translated by linear interpolation to 100 and 0% hematite-like absorption or 0 and 100% soot-like absorption.

A time-series of absorption coefficients separated for iron oxide and soot at 650 nm was calculated and is shown in Fig. 15. To prove the hypothesis that the spectral broad absorption is caused by soot, the SOAP filters were analysed by a Raman offline photometer, which is sensitive to graphitic carbon. A description of the Raman method is given in Mertes et al. (2004). In addition, filters collected using a PSAP onboard of the research aircraft Partenavia (Bierwirth et al. 2008) during the SAMUM-1 campaign were analysed.

Soot concentrations measured by Raman photometry are significantly higher than soot concentrations derived by SOAP. In some cases values of the soot concentration differ up to an order of magnitude. There are two possible explanations. First of all, it has to be considered that the Raman photometer is sensitive to graphitic carbon, and the calibration of the Raman photometer was done using soot (Monarch 71, Cabot Corporation). The absorption coefficients determined by the Raman method are thus valid for soot with the same ratio of total soot to graphitic carbon as it is for Monarch 71. In addition, a possible scattering artefact because of multiple scattering inside the filter was not accounted for. Test with soot (Monarch 71) and different amounts of purely scattering material (quartz) showed that the soot absorption is overestimated by the Raman method in presence of strongly scattering material on the filter. A quantification of this effect was not possible up to now. Thus, the calibration of the Raman photometer is not valid for the aerosol during Samum-1, and a quantification of the soot concentration using Raman photometry is not possible. Although a calibration is missing, the Raman method proves that there is soot in samples

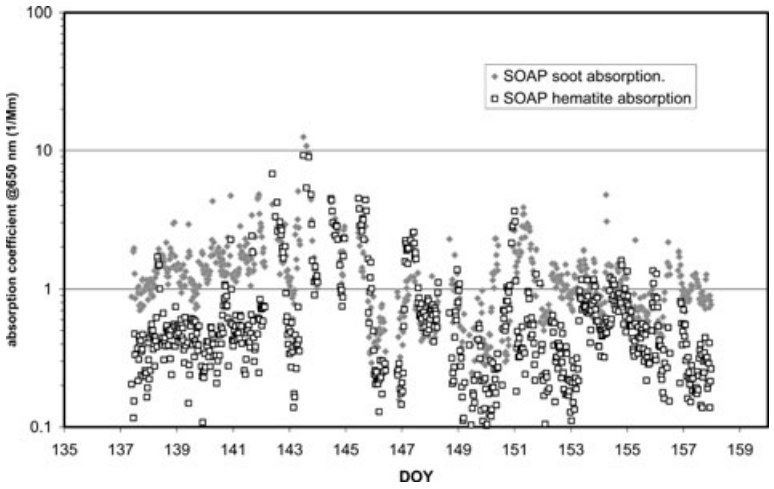

Fig. 15. Absorption coefficients at 650 nm split into soot and hematite absorption.

collected at the field station Zagora and onboard of the aircraft Partenavia.

3.4. Imaginary part of refractive index of the total aerosol and dust mode particles

The quantification of the two major absorbing components is used to investigate the optical properties of dust mode particles. The particle number size distributions were split into a fine and a dust mode (cf. Fig. 16). Using Mie scattering calculations, the relative soot fraction of the fine mode particles was estimated by variation of the soot concentration until the Mie-calculated absorption fits to the soot absorption, which was determined by the SOAP. This method is based on the assumption that the main components of the fine mode are sulphates (Kaaden et al., 2008), which is used as proxy for non-soot particles and soot with refractive indices of $m_{\text{sulph}} = 1.53 + 0\text{i}$ (Schladitz et al., 2008) and $m_{\text{soot}} = 1.75 + 0.44\text{i}$ (d'Almeida et al., 1991), respectively.

The absorption coefficient of fine mode particles is dominated by soot. Thus, a parametrization of the spectral absorption coefficient using eq. 20, with an Ångström absorption exponent of $\alpha = 1$ and the measured soot-absorption coefficient at 650 nm, allows to estimate the spectral absorption for fine mode particles. The dust mode absorption is given by the difference of the

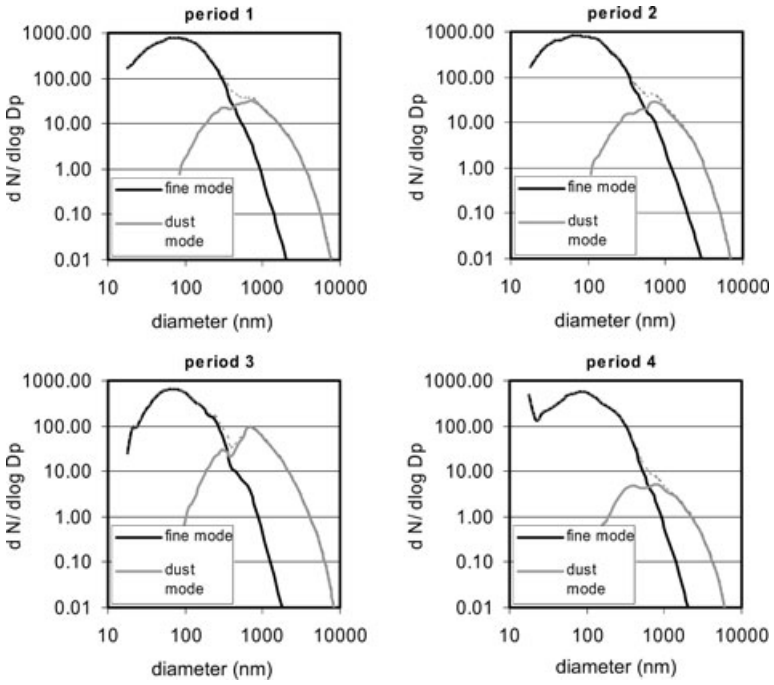

Fig. 16. Mode splitting for the four periods.

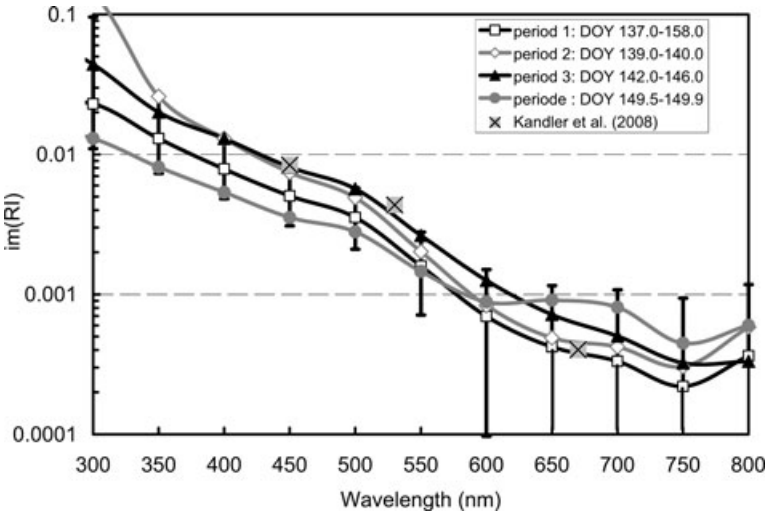

Fig. 17. Spectral imaginary part of refractive indices of dust mode particles for four time periods measured by SOAP. Also shown is the average refractive index over the entire measurement period for particles from particle diameters from 0.5 to 5.0 μm derived by electron microscopy (Kandler et al., 2008). Error bars are only shown for Period 1.

Table 1. Properties of fine and dust mode particles for four periods

		Period 1	Period 2	Period 3	Period 4
Volume fraction soot (%)	Fine & dust mode	0.25	0.41	0.08	0.28
	Fine mode	4.50	3.44	4.76	1.29
Volume conc. (μm^3 cm^{-3})	Fine mode	1.01	1.89	0.66	0.99
	Dust mode	18.64	14.23	38.76	3.82
Effective radius (μm)	Fine mode	0.18	0.15	0.11	0.13
	Dust mode	0.90	0.65	0.86	0.94
Ångström exponent	Fine mode	1.18	1.07	1.17	1.31
	Dust mode	6.09	6.37	6.51	3.65
Refractive index of dust mode particles at 650 nm	Real part	1.53	1.53	1.53	1.53
	Imaginary part	0.0045	0.0034	0.0048	0.0013

measured total absorption and the soot absorption by

$$\sigma_{\mathrm{abs,dust}}(\lambda) = \sigma_{\mathrm{abs}}(\lambda) - \sigma_{\mathrm{abs,soot}}(650\ \mathrm{nm}) \cdot \left(\lambda/650\ \mathrm{nm}\right)^{-\alpha}. \quad (21)$$

The RI-inversion was used to calculate the spectral imaginary part of dust mode particles. The spectral imaginary parts are shown in Fig. 17. In contrast to the imaginary part of the refractive index of the total aerosol shown in Fig. 13, the spectral run is similar for all periods. This result leads to the conclusion that the relative iron oxide concentration in the dust mode is relatively constant for all four periods. Similar results are reported by Kandler et al. (2008). The results of the mode fitting, the relative volume fraction of soot and the refractive indices of dust mode particles at a wavelength of 650 are summarized in Table 1. Spectral imaginary parts of the refractive indices are given in Table 2 for the total and dust mode aerosol.

3.5. *Uncertainties of absorption coefficients and derived refractive indices*

The uncertainty of the imaginary part of refractive indices depends on uncertainties of the input parameters for the RI-inversion method. The input parameters are the particle number size distribution, the real part of the refractive index and the absorption coefficient. The relative uncertainty of the particle number size distribution was estimated to 12% (Schladitz et al., 2008). This uncertainty results in an error of 8–14% of the imaginary part of the refractive index over the entire spectral range from 300 to 800 nm. In Schladitz et al. (2008), it was shown that a real part of refractive index of about 1.53 is a reasonable estimate. An error of 5% in the real part results in an error of 3–7% in the spectral range from 300 to 800 nm.

The uncertainty of the absorption coefficient measured with the SOAP is between 0.3 and 0.6 Mm^{-1}. This uncertainty was determined for an averaging time of 10 min and is mainly caused by the photon noise. The time periods investigated in this study have averaging times of more than 9 h, reducing the error of the photon noise by a factor of about seven. We use for a worst-case estimate an uncertainty of 0.3 Mm^{-1}, resulting in an average relative error of 15% for the entire field campaign.

Another source of errors is the cross sensitivity to particle scattering. Bond et al. (1999) stated a cross sensitivity and uncertainty of 2 ± 2% of the scattering for a PSAP. In a laboratory

Table 2. Imaginary part of refractive indices (k) and uncertainties ($\pm\Delta k$) for the average aerosol over the entire field campaign (Period 1)

	Total aerosol			Dust mode		
Wavelength (nm)	Mean k	$+\Delta k$	$-\Delta k$	Mean k	$+\Delta k$	$-\Delta k$
300	0.029	0.06	0.014	0.023	0.073	0.012
350	0.017	0.017	0.0067	0.013	0.013	0.0057
400	0.011	0.0077	0.0041	0.0079	0.0053	0.0031
450	0.0074	0.0045	0.0027	0.0051	0.0029	0.0020
500	0.0057	0.0032	0.0020	0.0035	0.0022	0.0014
550	0.0034	0.0021	0.0014	0.0016	0.0012	0.0009
600	0.0024	0.0015	0.0011	0.0007	0.0008	0.0006
650	0.0020	0.0013	0.0009	0.0005	0.0007	0.0005
700	0.0019	0.0014	0.0009	0.0003	0.0007	0.0004
750	0.0018	0.0013	0.0009	0.0002	0.0007	0.0003
800	0.0019	0.0014	0.0009	0.0004	0.0008	0.0004

test using ammonium sulphate and quartz, it was shown that the cross sensitivity to scattering was reduced by the SOAP method to values between 0.5% and 1%. For an error estimation, we used the worst case of 1% cross sensitivity to scattering. In the spectral range from 600 to 800 nm, the measured absorption coefficient typically is in the same order of magnitude as the cross sensitivity to scattering. Thus, the uncertainty in the derived imaginary part of refractive index can be up to 100%.

All these uncertainties result in an uncertainty of the imaginary part of the refractive index, which is given in Table 2.

3.6. *Correlation between optical properties and particle number size distribution*

A correlation analysis was done to show the relation between particle number size concentrations of fine and dust mode particles to the absorption and scattering coefficients. The size resolved coefficient of determination spectrum (*CDS*) for absorption and scattering is defined by the Pearson coefficient of determination (R^2) by

$$CDS_X(d_\mathrm{p}) := R^2(n(d_\mathrm{p}), \sigma_X) \ , \tag{22}$$

with $X = \{\mathrm{abs}, \mathrm{sca}\}$. The coefficient of determination is the fraction of the variance in σ_X that can be explained by the number concentration $n(d_\mathrm{p})$ of the particle number size distribution at diameter d_p.

The results of the correlation analysis are shown in Fig. 18. The particle scattering is well correlated with particles larger than 1 μm in diameter with a maximum value of the coefficient of determination of about 0.9 at 1.6 μm. This result is in agreement with the effective radius reported by Schladitz et al. (2008). Particles smaller 0.5 μm are not correlated with the particle

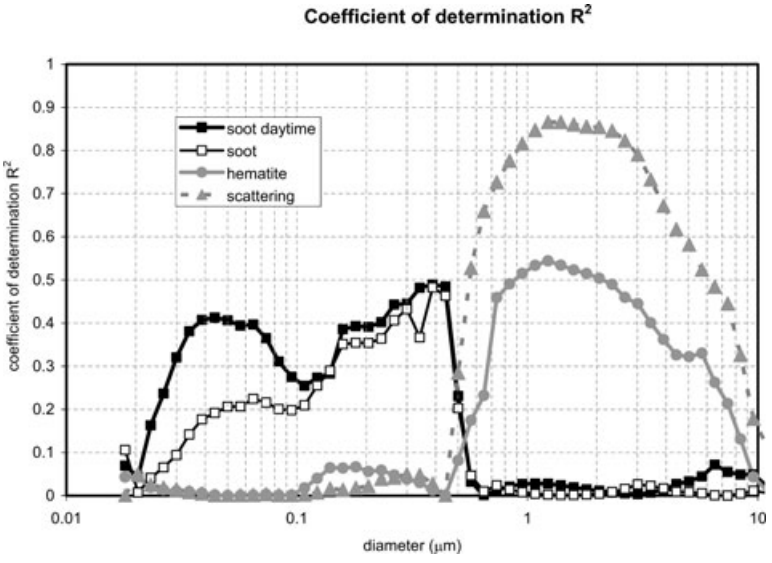

Fig. 18. Size resolved correlation spectrum of absorption and scattering. Shown are the correlations of absorption and scattering coefficients with the particle number concentration for each size. Black line with filled squares: daytime (06:00 to 18:00) soot absorption (650 nm); black line with open squares: soot absorption; grey line with filled circles: dust (hematite-like) absorption (650 nm); grey line with open triangles: total scattering (550 nm).

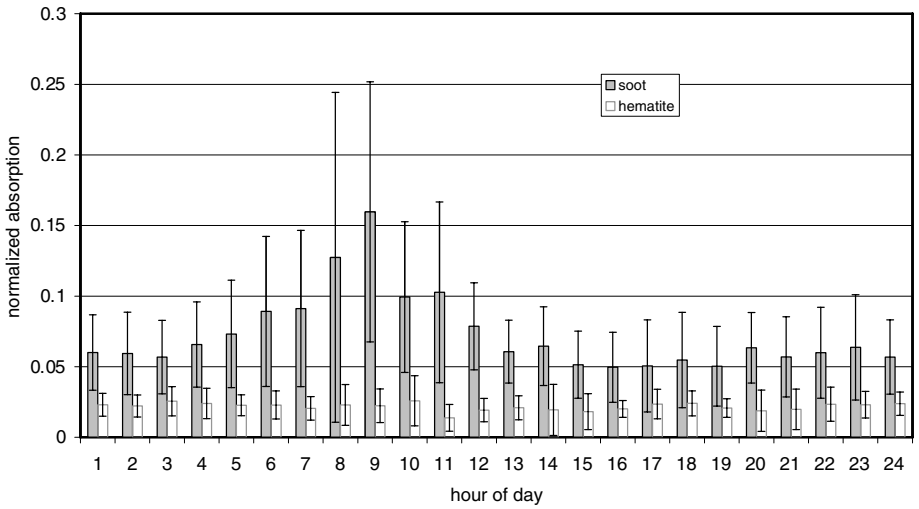

Fig. 19. Diurnal variation of normalized soot and hematite absorption at 650 nm. The error bars are the standard deviation of the hourly mean values for the entire period of 21 d. Only values for hematite absorption smaller 40 Mm^{-1} were used to exclude sand storms.

scattering coefficient. For the iron oxide absorption, we get a similar size-dependent coefficient of determination spectrum but with values lower than $R^2 = 0.5$. Scattering and iron oxide absorption spectra are well correlated with the dust mode, but almost no correlation to the fine mode was found. With these findings, we can identify the dust mode to be the particle fraction, which contains almost all iron oxides. This finding is in agreement with the result of the size resolved electron microscopy given by Kandler et al. (2008).

The soot absorption coefficient is correlated with the fine particle fraction. For dust and soot absorption, the maximum values of the coefficient of determination are around 0.5, and thus, we can state that soot and hematite can be found in well-separated modes. For daytime values, we can observe that there is a distinct maximum for the correlation of soot and particle number concentration at particle diameters of about 0.04 μm, which is a strong indication of externally mixed soot particles.

3.7. Discussion

Mineral dust and soot absorption coefficients were divided by the total particle scattering coefficient. The diurnal variations of these normalized absorptions are shown in Fig. 19. The soot absorption shows its lowest values from midnight to the early morning with average values of 0.8 Mm^{-1} and a strong increase in the morning hours. The data shown in Figs. 15 and 19 suggest that there is soot mixed in the Saharan background aerosol with respective soot-absorption coefficients between 0.5 and 1 Mm^{-1}. The presence of anthropogenic sulphate was shown by Kaaden et al. (2008) supporting the hypothesis of an anthropogenic influenced background aerosol. Local sources of soot could be the road traffic near the measurement station, the hotel in a distance of about 50 m or small villages in the vicinity of the measurement station. Another source of soot could be the furnaces of a pottery in Tamegrout, a village about 10 km northwest of the measurement station at Tinfou.

Imaginary parts of the refractive index at a wavelength of 700 nm are in the range ($k + \Delta k$ to $k - \Delta k$) from -0.0001 to 0.001 for dust mode particles and in the range from 0.001 to 0.0034 for the total aerosol. Values for the imaginary part of refractive index determined by airborne observation (Petzold et al., 2008) are between 0.0003 and 0.0025. For dust mode particles the values derived by the SOAP are slightly smaller than the airborne observations. This result can be explained by the soot correction of SOAP data. A similar method was not applied to any other measurement.

Imaginary parts of refractive indices also were determined with a Multi Angle Absorption Photometer (MAAP), using the same aerosol inlet as for the SOAP (Schladitz et al., 2008). The data of MAAP were not corrected for soot absorption. The imaginary part of the refractive index measured with MAAP at a wavelength of 630 nm is $k = 0.0031$. This value is higher than the respective values measured with the SOAP for mineral dust particles ($k = 0.0004$) and for the total aerosol ($k = 0.002$). The differences of the imaginary parts of refractive indices of these three studies can be explained by different methods, whereby only the method using the SOAP data can distinguish between soot and dust absorption.

4. Conclusion

Spectral absorption coefficients were measured using a new spectral absorption photometer in the spectral range from 300 to 800 nm with a resolution of 50 nm. A ray-tracing method was

developed to correct for a loading-dependent sensitivity and a cross sensitivity to particle scattering for fibre filter based absorption photometers.

A method based on the spectral features of an iron oxide such hematite was used to apportion absorption coefficients into absorption by soot and absorption by mineral dust. An independent measurement of graphitic carbon using the Raman method confirms the presence of soot on filter samples measured during the SAMUM-1 field study.

A correlation analysis with the particle number size distributions pointed out that the soot-like absorption is correlated with particles smaller than 500 nm in diameter, and the dust absorption is correlated with particles larger than 500 nm.

Using Mie scattering calculations, refractive indices were derived in the spectral range from 300 to 800 nm for the total aerosol and a dust mode aerosol. Average imaginary parts of refractive indices in the wavelength range from 300 to 800 nm are between 0.029 to 0.0018 and 0.023 to 0.0002 for the total aerosol and the mineral dust aerosol, respectively. Refractive indices of dust mode particles are significantly lower for wavelengths larger than 550 nm compared with values given in literature (e.g. Sokolik and Toon 1999; Hess et al. 1998).

5. Acknowledgments

This study was supported by the German Research Foundation (DFG contract MU2669/1-1) and (DFG contract FOR 539) in the framework of the research group SAMUM.

References

Alfaro, S. C., Lafon, J. L., Formenti, P., Goudichet, A. and Maille, M. 2004. Iron oxides and light absorption by pure desert dust: an experimental study. *J. Geophys. Res.* **109**, D08208.

d'Almeida, G. A., Koepke, P. and Shettle, E. P. 1991. *Atmospheric Aerosols: Global Climatology and Radiative Characteristics*. A. Deepak Publishing, Hampton, VA.

Anderson, T. L., Covert, D. S., Marshall, S. F., Laucks, M. L., Charlson, R. J. and co-authors. 1996. Performance characteristics of a high-sensitivity, three-wavelength, total scatter/backscatter nephelometer. *J. Atmos. Ocean. Technol.* **13**, 967–986.

Arimoto, R., Balsam, W., Schloesslin, C. 2002. Visible spectroscopy of aerosol particles collected on filters: iron-oxide minerals. *Atmos. Environ.* **36**, 89–96.

Arnott, W. P., Hamasha, K., Moosmüller, H., Sheridan, P. J. and Ogren, J. A. 2005. Towards aerosol light-absorption measurements with a 7-wavelength aethalometer: evaluation with a photoacoustic instrument and 3-wavelength nephelometer. *Aerosol Sci. Technol.* **39**, 17–29.

Ångström, A. 1964. The parameters of atmospheric turbidity. *Tellus* **16**, 64–75.

Balkanski, Y., Schulz, M., Claquin, T. and Guibert, S. 2007. Reevaluation of mineral aerosol radiative forcings suggests a better agreement with satellite and AERONET data. *Atmos. Chem. Phys.* **7**, 81–95.

Bierwirth, E., Wendisch, M., Ehrlich, A., Heese, B., Otto, S. and co-authors. 2008. Spectral surface albedo over Morocco and its impact on the radiative forcing of Saharan dust. *Tellus* **61B**, doi:10.1111/j.1600-0889.2008.00395.x.

Birmili, W., Stratmann, F. and Wiedensohler, A. 1999. Design of a DMA-based size spectrometer for a large particle size range and stable operation. *J. Aerosol Sci.*, **30**, 549–553.

Bond, T. C., Anderson, T. L. and Campbell, D. 1999. Calibration and intercomparison of filter-based measurements of visible light absorption by aerosols. *Aerosol Sci. Technol.*, **30**, 582–600.

Collaud Coen, M., Weingartner, E., Schaub, D., Hueglin, C., Corrigan, C. and co-authors. 2004. Saharan dust events at the Jungfraujoch: detection by wavelength dependence of the single scattering albedo and analysis of the events during the years 2001 and 2002. *Atmos. Chem. Phys.* **4**, 2465–2480.

Fialho, P., Freitas, M. C., Barata, F., Vieira, B., Hansen, A. D. A. and co-authors. 2006. The Aethalometer calibration and determination of iron concentration in dust aerosols. *J. Aerosol Sci.* **37**, 1497–1506.

Hansen, A. D. A., Rosen, H. and Novakov, T. 1984. The aethalometer–an instrument for the realtime measurement of optical absorption by aerosol particle. *Sci. Total Environ.* **36**, 191–196.

Haywood, J. and Bougher, O. 2000. Estimates of the direct and indirect radiative forcing due to tropospheric aerosols: a review. *Rev. Geophys.* **38**, 513–543.

Haywood, J. M., Francis, P. N., Glew, M. D. and Taylor, J. P. 2001. Optical properties and direct radiative effect of Saharan dust- a case study of two Saharan dust outbreaks using aircraft data. *J. Geophys. Res.* **106**(D16), 18 417–18 430.

Haywood, J., Francis, P., Osborne, S., Glew, M., Loeb, N. and co-authors. 2003. Radiative properties and direct radiative effect of saharan dust measured by the c-130 aircraft during SHADE: 1. Solar spectrum. *J. Geophys. Res*. **108**, 8577.

Henyey, L. and Greenstein, J. 1941. Diffuse radiation in the galaxy. *Astrophys. J.* **93**, 70–83.

Hess, M., Koepke, P. and Schult, I. 1998. Optical properties of aerosols and clouds: the software package OPAC. *Bull. Am. Meteorol. Soc.* **79**, 831–844

IPCC, 2007. *Climate Change 2007. The Physical Science Basis. Contribution of Working Group 1 to the Fourth Assessment Report of the Intergovernmental Panel on Climate Change (IPCC)* (eds. A. S. Solomon, D. Qin, M. Manning, M. Marquis, K. Averyt and co-editors). Cambridge University Press, Cambridge.

Kaaden, N., Massling, A., Schladitz, A., Müller, T., Kandler, K. and co-authors. 2008. State of mixing, shape factor, number size distribution, and hygroscopic growth of the saharan anthropogenic and mineral dust aerosol at Tinfou, Morocco. *Tellus* **61B**, doi:10.1111/j.1600-0889.2008.00388.x.

Kandler, K., Schütz, L., Deutscher, C., Hofmann, H., Jäckel, S. and co-authors. 2008. Size distribution, mass concentration, chemical and mineralogical composition, and derived optical parameters of the boundary layer aerosol at Tinfou, Morocco, during SAMUM 2006. *Tellus* **61B**, doi:10.1111/j.1600-0889.2008.00385.x.

Kaufman, Y. J., Koren, I., Remer, L.A., Tanre, D., Ginoux, P. and co-authors. 2005. Dust transport and deposition observed from the Terra-Moderate Resolution Imaging Spectroradiometer (MODIS) spacecraft over the Atlantic Ocean. *J. Geophys. Res.* **110**, 1–16.

Linke, C., Möhler, O., Veres, A., Mohácsi, Á., Bozóki, Z. and co-authors. 2006. Optical properties and mineralogical composition of different Saharan mineral dust samples: a laboratory study. *Atmos. Chem. Phys.* **6**, 3315–3323.

Mertes, S., Dippel, B. and Schwarzenböck, A. 2004. Quantification of graphitic carbon in atmospheric aerosol particles by Raman spectroscopy and first application for the determination of mass absorption efficiencies. *J. Aerosol Sci.* **35**, 347–361.

Petzold, A., Rasp, K., Weinzierl, B., Esselborn, M., Hamburger, T. and co-authors. 2008. Saharan dust refractive index and optical properties from aircraft-based observations during SAMUM 2006. *Tellus* **61B**, doi:10.1111/j.1600-0889.2008.00383.x.

Prahl, S. A., Keijzer, M., Jacques, S. L. and Welch, A. J. 1989. A Monte Carlo model of light propagation in tissue. *SPIE Inst. Ser. IS*. **5**, 102–111.

Schladitz, A., Müller, T., Massling, A., Kaaden, N., Kandler, K. and co-authors. 2008. In situ measurements of Optical Properties at Tinfou (Morocco) during the Saharan Mineral Dust Experiment SAMUM 2006. *Tellus* **61B**, doi:10.1111/j.1600-0889.2008.00397.x.

Schmid, O., Artaxo, P., Arnott, W. P., Chand, D., Gatti, L. V. and co-authors. 2006. Spectral light absorption by ambient aerosols influenced by biomass burning in the Amazon Basin, I: vomparison and field calibration of absorption measurement techniques. *Atmos. Chem. Phys.* **6**, 3443–3462.

Shettle, P. and Fenn, R. 1979. Models for the aerosol of the lower atmosphere and the effects of humidity variations on their optical properties. AFCRL Technical Report 79 0214, Research Papers No.676, Air Force Cambrige Research Laboratory.

Sokolik, I. N. and Toon, O. B. 1996. Direct radiative forcing by anthropogenic airborne mineral aerosols. *Nature* **381**, 681–683.

Sokolik, I. N. and Toon, O. B. 1999. Incorporation of mineralogical composition into models of the radiative properties of mineral aerosol from UV to IR wavelength. *J. Geophys. Res.* **104**, 9423–9444.

Tegen, I., Lacis, A. A. and Fung, I. 1996. The influence of mineral aerosols from disturbed 907 soils on the global radiaton budget. *Nature* **380**, 419–422.

Virkkula, A., Ahlquist, N. C., Covert, D. S., Arnott, W. P., Sheridan, P. J. and co-authors. 2005. Modification, calibration and a field test of an instrument for measuring light absorption by particles. *Aerosol Sci. Technol.* **39**, 68–83.

Weingartner, E., Saathof, H., Schnaiter, M., Streit, N., Bitnar, B. and co-authors. 2003. Absorption of light by soot particles: determination of the absorption coefficient by means of Aethalometers. *J. Aerosol Sci.* **34**, 1445–1463.